Biosensors and Bioelectronics 142 (2019) 111594

Contents lists available at ScienceDirect

Biosensors and Bioelectronics

journal homepage: www.elsevier.com/locate/bios

Nano-Fe_3C@PGC as a novel low-cost anode electrocatalyst for superior performance microbial fuel cells

Meihua Hu[a], Xin Li[a], Juan Xiong[a], Lizhen Zeng[a], Yingshan Huang[a], Yuping Wu[a,b,c], Guozhong Cao[d,**], Weishan Li[a,b,*]

[a] School of Chemistry and Environment, South China Normal University, Guangzhou, 510631, China
[b] National and Local Joint Engineering Research Center of MPTES in High Energy and Safety LIBs, Engineering Research Center of MTEES (Ministry of Education), Key Lab. of ETESPG(GHEI), South China Normal University, Guangzhou, 510006, China
[c] School of Energy Science and Engineering, Nanjing Technology University, Nanjing, 211816, China
[d] Department of Materials Science and Engineering, University of Washington, Seattle, WA, 98195, United States

ARTICLE INFO

Keywords:
Iron carbide
Porous graphitized carbon
Electrocatalyst
Anode
Microbial fuel cells

ABSTRACT

We report a novel anode electrocatalyst, iron carbide nanoparticles dispersed in porous graphitized carbon (Nano-Fe_3C@PGC), which is synthesized by facile approach involving a direct pyrolysis of ferrous gluconate and a following removal of free iron, but provides microbial fuel cells with superior performances. The physical characterizations confirm the unique configuration of iron carbide nanoparticles with porous graphitized carbon. Electrochemical measurements demonstrate that the as-synthesized Nano-Fe_3C@PGC exhibits an outstanding electrocatalytic activity toward the charge transfer between bacteria and anode. Equipped with Nano-Fe_3C@PGC, the microbial fuel cells based on a mixed bacterium culture yields a power density of 1856 mW m^{-2}. The resulting excellent performance is attributed to the large electrochemical active area and the high electronic conductivity that porous graphitized carbon provides and the enriched electrochemically active microorganisms and enhanced activity towards the redox reactions in microorganisms by Fe_3C nanoparticles.

1. Introduction

Microbial fuel cells (MFCs) can recover energy from substances through electrochemically active bacteria, giving rise to their promising potential for wastewater treatment and green electricity generation (Logan and Rabaey, 2012; Sun et al., 2016; Wang et al., 2016b). Therefore, MFCs have been attracting considerable attention in recent years (Choi, 2015; Santoro et al., 2017). Nevertheless, the relatively low power output and the difficulty in achieving affordable electrode materials remain the barriers for the further advancement of MFCs and their wide-spread and large-scale application (Choi, 2015; Zhao et al., 2009).

The performance of MFCs relies critically on extracellular electron transfer (EET) between intracellular respiratory chains of electrochemically active bacteria (EAB) and extracellular anodes, which requires an electrochemically active biofilm that attaches to the anode surface and electron transfer mediators such as c-type cytochromes (c-Cyts) in electrochemically active bacteria(Liu et al., 2018; Sonawane et al., 2017; Zeng et al., 2018). For the further enhancing performance of MFCs, it is essential to develop suitable anode materials, which are required with various characters, such as large surface area, excellent electronic conductivity, and high electrocatalytic activity towards electron transfer mediators (Cui et al., 2014; Feng et al., 2014; Wang et al., 2015b).

In these regards, porous carbon has been widely acknowledged to be the favorable anode material for MFCs because of its remarkable stability, good electronic conductivity, availability, and ease functionalization(Xiong et al., 2018; Zou et al., 2016). The reported porous carbon materials include ordered mesoporous carbon (Qiao et al., 2010) and porous carbon with defined pore size (Chen et al., 2015; Li et al., 2017). Furthermore, the performance improvement of carbon materials could be achieved by high graphitization (Xiong et al., 2018) and functionalization with N, O, and S-doping (Niu et al., 2018; Yu et al., 2015). Unfortunately, carbon materials reported up to date still present low activity for the electron transfer mediators in the electrochemically active biofilm.

Some transition metal carbides exhibit electrocatalytic activity toward various reactions(Xiao et al., 2016; Zeng et al., 2018). Among

* Corresponding author. School of Chemistry and Environment, South China Normal University, Guangzhou, 510631, China.
** Corresponding author.
E-mail addresses: gzcao@u.washington.edu (G. Cao), liwsh@scnu.edu.cn (W. Li).

https://doi.org/10.1016/j.bios.2019.111594
Received 25 May 2019; Received in revised form 20 July 2019; Accepted 11 August 2019
Available online 13 August 2019
0956-5663/

these carbides, iron carbide (Fe_3C) is most attractive because of its excellent thermal stability and mechanical strength, especially the abundant resources of iron(Guan et al., 2016; Xiao et al., 2016). It has been used as electrode materials for electrochemical energy storage and electrocatalysts for oxygen reduction reaction. Su et al. reported a core–shell structured Fe@Fe_3C/C composite as an anode for lithium ion battery, which exhibited a high reversible capacity, stable cycling performance, and improved initial efficiency (Su et al., 2013). Hu et al. presented Fe_3C-functionalized graphene composite as an electrocatalyst that revealed excellent activity and stability for oxygen reduction reaction in alkaline solution, which was comparable to the commercial Pt/C catalyst (Hu et al., 2014). Up to date, however, Fe_3C has never been considered as anode electrocatalyst for MFCs.

Various exoelectrogenic bacteria, such as *Escherichia coli* (Wang et al., 2014), *Geobacter sulfurreducens* (Malvankar et al., 2012), *Shewanella* (Wei et al., 2016) and *Klebsiella pneumoniae* (Zhang et al., 2009) have been used in MFCs. Quite recently, mixed microbial communities have drawn more attention, because a mixed bacterial culture is readily available, pragmatic, and nutrient adaptable compared to a pure culture (Kawale et al., 2017; Samsudeen et al., 2015).

In this study, we report a novel anode electrocatalyst for improving power density of MFCs, which is prepared by directly pyrolysing ferrous gluconate and acid-etching free iron, and presents a unique configuration: iron carbide nanoparticles dispersed in porous graphitized carbon (Nano-Fe_3C@PGC). The performances of the resulting Nano-Fe_3C@PGC were evaluated in MFCs based on mixed bacteria. The combination of porous graphitized carbon with Fe_3C nanoparticles provides simultaneously the electrocatalytic activity and the electronic conductivity, resulting in an excellent power density output of the MFCs. Considering its synthesis facileness, low-cost raw materials and outstanding electrocatalytical activity, the resulting Nano-Fe_3C@PGC provides a promising anode electrocatalyst for the practical application of high-performance MFCs.

2. Experimental section

2.1. Materials preparation

In our previous work (Xiong et al., 2018), we reported porous graphitic carbon (PGC) as anode for MFCs. The PGC was synthesized via the solid-state pyrolysis of ferrous gluconate following by completely removing all the iron compositions. Further investigations revealed that a novel configuration, iron carbide nanoparticles dispersed in porous graphitized carbon (Nano-Fe_3C@PGC), could be obtained by removing free iron but leaving Fe_3C on PGC. Specially, the Nano-Fe_3C@PGC composite was prepared by using iron D-gluconate dihydrate (Alladin, 98%). Firstly, the ferrous gluconate was carbonized at 900 °C for 2 h with a heating rate of 2 °C min^{-1} and a pure argon flow (10–20 mL min^{-1}). Subsequently, for removal of residual iron metal, the resulting product (Fe–Fe_3C@PGC) was treated by 5 wt% HCl for 15 min. After rinsing with ultrapure water and drying in 80 °C, Nano-Fe_3C@PGC was synthesized. For comparison, pure porous graphitic carbon (PGC) was also prepared by completely removing all the iron compositions. For understanding the formation mechanism of the electrocatalyst, various temperatures (500–900 °C) for the carbonization of ferrous gluconate were also considered. The materials characterizations measurements were described in Supplementary Materials (S1.1).

2.2. Electrochemical measurements

The electrochemical performances of the resulting electrocatalysts were characterized on Bio-logic VMP-3 (Bio-Logic SAS, France). All these measurements were performed with a three-electrode cell (Fig. S1a) consisting of working electrode with electrocatalysts (4 cm^2), a platinum-wire as counter electrode, and a saturated calomel electrode (SCE) as reference electrode. Working electrode was prepared by dispersing electrocatalysts in 10 wt% poly tetrafluoroethylene solution (PTFE) and coating the mixture on carbon felt (CF). In chronoamperometry, working electrode was kept at 0.2 V (*vs.* SCE) and the corresponding current was recorded. Constant-current discharge experiments were performed at 0.1 μA after stable biofilms had formed. Cyclic voltammetry was carried out from −0.6 V to 0.3 V (*vs.* SCE) at 1 mV s^{-1}. The electrochemical impedance spectroscopy was performed at open circuit potential from 10^5 to 10^{-2} Hz with a sinusoidal perturbation of 5 mV.

2.3. MFCs assembly and operation

An air-cathode single-chamber MFCs (Fig. S1b) with a liquid volume of 28 mL was assembled as previously reported (Zeng et al., 2018). Anode was prepared as the working electrode. Cathode was prepared using a catalyst of Pt/C (0.5 mg cm^{-2}, InnoChem, China), which was mixed with 30 μL water, 67 μL Nafion solution (5 wt%, Dupont) and 116 μL ethanol. The resulting slurry was coated onto one side of carbon cloth (Yuan et al., 2013).

To start up experiments, the MFCs were initially inoculated by 5.0 mL pre-acclimated bacteria from matured MFCs (originally inoculated with activated anaerobic sludge) and 23 mL acetate medium solution. The compositions of the medium solution were described in Supplementary Materials (S1.2). MFCs were operated with a 1000 Ω external loading resistance. A data acquisition system (PS2024, Smacq, China) was used to record the cell voltage. When the voltage decreased to less than 0.05 V, 80% medium solution was replaced for one operation.

Polarization curves were obtained by linear sweep voltammetry at 1 mV s^{-1}. The power density, P (W m^{-2}), was obtained based on P = IU/A (Chen et al., 2015), where I (A) is the current, U (V) the voltage of the MFCs and A (m^2) the projected area of the anode (4.0 cm^2). To ensure the reproducibility of the experimental results, all the tests were conducted in triplicate, and the reported value was the mean one in the triplicate tests with an error of less than 1%.

3. Results and discussion

3.1. Structural and morphology of Nano-Fe_3C@PGC

The synthetic strategy of Nano-Fe_3C@PGC is schematically illustrated in Fig. 1a, which requires delicate controlling of the temperature for pyrolysis and the acid concentration for iron removal. As evidenced by the XRD and FTIR spectra of the ferrous gluconate pyrolyzed at different temperature (Figs. S2 and S3), at a pyrolysis temperature below 800 °C, Fe_xC encapsulated in carbon is obtained, but the carbon is amorphous and Fe_3C nanoparticles cannot be formed. With a concentrated acid solution, Fe_3C is removed completely. Fig. 1b shows a SEM image of the resulting Nano-Fe_3C@PGC, which consists of porous nanorod with dispersed Fe_3C nanoparticles. The formation mechanism of Nano-Fe_3C@PGC can be explained by thermogravimetric analysis (TGA) of ferrous gluconate (Fig. S4) and illustrated schematically in Fig. S5. Pores cannot be observed from the sample without acid treatment (Fe–Fe_3C@PGC, Fig. S6a), but are present clearly in Nano-Fe_3C@PGC, with their sizes ranging from 10 to 200 nm (Fig. S6b). These observations suggest that the pores in Nano-Fe_3C@PGC are formed from the removal of iron metal from Fe–Fe_3C@PGC during etching. The porous graphitic carbon can be more clearly identified when Fe_3C is also removed (PGC, Fig. S6c). TEM images (Fig. 1c) indicates that the size of the Fe_3C nanoparticles is about 100 nm. The lattice lines, 0.21 nm corresponding to (211) lattice plane of Fe_3C and 0.34 nm for (002) lattice plane of graphitic carbon, are observed from the HRTEM image (Fig. 1d). Elemental mapping (Fig. S7) reveals that the carbon is distributed uniformly, and the iron is scattered in nanoparticles.

XRD patterns (Fig. 2a) show a diffraction peak at 2θ = 26.6° in both

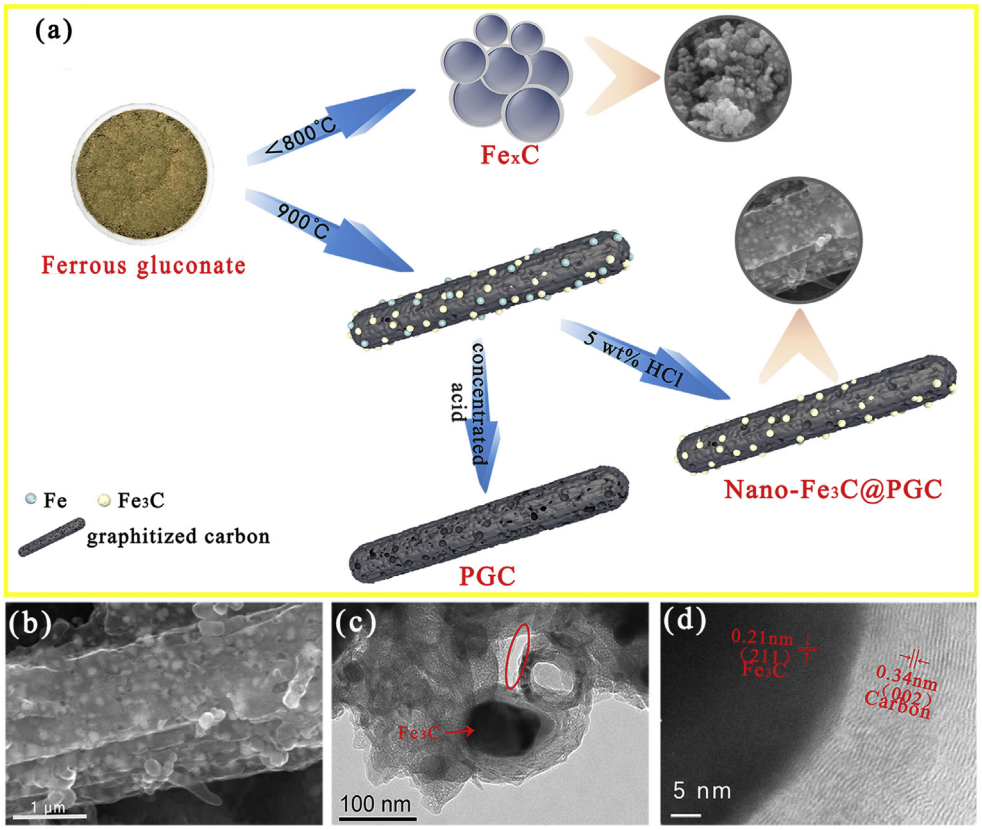

Fig. 1. (a) Schematic preparation of Nano-Fe_3C@PGC from ferrous gluconate. Morphological and structural characterizations of Nano-Fe_3C@PGC: (b) SEM, (c) TEM, and (d) HRTEM images.

PGC and Nano-Fe_3C@PGC samples, which can be indexed to (002) lattice plane of graphitic carbon (C, JCPDS 99–0057), indicating that the precursor was well-graphitized under high-temperature. Other diffraction peaks in Nano-Fe_3C@PGC sample, can be well indexed to cohenite Fe_3C (JCPDS 35–0772). But for Fe–Fe_3C@PGC, there exists a sharp characteristic peak at $2\theta = 44.6^\circ$ indexed to (110) lattice plane of α-Fe (Fe, JCPDS 06–0696), indicating the presence of residual iron metal in the sample. After hydrochloric acid leaching, diffraction peak of Fe metal disappears, implying that the iron metal has been successfully removed. Energy-dispersive x-ray spectra (EDS) of these materials (Fig. S8) show that the content of Fe decreases after hydrochloric acid leaching, which is in accord with XRD results.

Raman spectra (Fig. 2b) of samples display the characteristic peaks at 1326 cm^{-1} for D-band, 1594 cm^{-1} for G-band and a weak broad band at 2681 cm^{-1} for 2D peaks, confirming that the carbon in these samples exhibit graphitic and amorphous structures (Dresselhaus et al., 2010; Sun et al., 2018). Two low-intensity peaks located at 221 and 285 cm^{-1} are indexed to Fe_3C (Liao et al., 2013). G-band observed in Raman spectra is indicative of highly developed graphitic carbon (Ferrari, 2007). The relative intensity ratio of G-band and D-band (I_G/I_D) is another indication of high degree of graphitization (Wang et al., 2016a). The I_G/I_D ratio of 0.795 in Fe–Fe_3C@PGC increases to 1.545 in Nano-Fe_3C@PGC and 1.634 in PGC when iron metal is removed. The increased I_G/I_D value suggests that the acid treatment also remove some amorphous carbon, implying that the Nano-Fe_3C@PGC has a relatively high degree graphitization. The graphitized carbon provides Nano-Fe_3C@PGC with high electronic conductivity, which is beneficial for electron transfer between anode and biofilm.

The main peaks of FTIR (Fig. 2c) at around 600 cm^{-1}, 1250 cm^{-1}, 1600 cm^{-1}, and 3450 cm^{-1}, represent Fe–C group, C–O group, C=O group, and O–H group, respectively(Mian and Liu, 2019). The Fe–C functional group cannot be identified in PGC, while O-containing functional groups remains in Nano-Fe_3C@PGC, which are beneficial for improving electrochemical active area (Chen et al., 2016).

The N_2 adsorption-desorption isotherms of all the samples (Fig. S10) indicate that their adsorption/desorption behaviors belong to typical type IV. The specific surface area calculated by the BET method are shown in Table S1. The specific surface area is in the order of PGC (234 $m^2 g^{-1}$), Nano-Fe_3C@PGC (169 $m^2 g^{-1}$) and Fe–Fe_3C@PGC (110 $m^2 g^{-1}$), indicating that the pores in the samples are formed from the removal of the iron-containing species. Large specific surface area of materials is beneficial for the access of medium solution and thus helps improve power output of MFCs. As demonstrated below, however, Nano-Fe_3C@PGC has the smallest specific surface area but provides MFCs with the largest power density, suggesting that Fe_3C in Nano-Fe_3C@PGC plays an important role in the charge transfer between anode and biofilm.

The thermogravimetric analysis was carried out to measure the Fe content of Nano-Fe_3C@PGC. The obtained result is presented in Fig. 2d, the minor weight loss from 30 to 485 °C (2.72 wt%) can be ascribed to the removal of the oxygen-containing groups, while the major weight loss from 485 to 700 °C is credited to the oxidation of Fe_3C and carbon. Eventually, PGC becomes CO_2 gas and Fe_3C is accordingly oxidized to Fe_2O_3 (Wang et al., 2015a). The loading quantity of Fe_3C nanoparticles (x wt%) can be calculated based on Equation (1):

$$x = \frac{2}{3} \times \frac{m_2}{m_1} \times \frac{M_a}{M_b} \times 100\% \quad (1)$$

where m_1 and m_2 are the mass of original Nano-Fe_3C@PGC and the residual Fe_2O_3, M_a and M_b are the molecular mass of Fe_3C and Fe_2O_3, respectively. The calculated Fe_3C content in Nano-Fe_3C@PGC is 20.1 wt %.

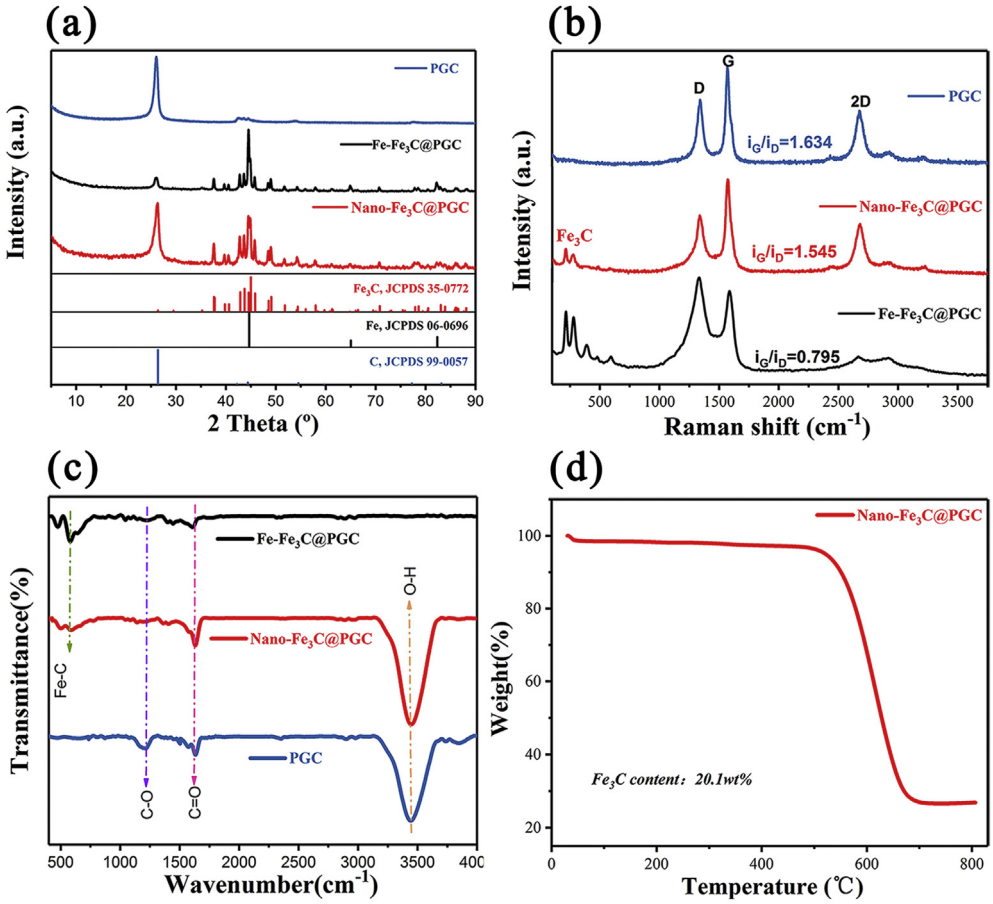

Fig. 2. The characterizations of the Fe–Fe_3C@PGC, Nano-Fe_3C@PGC and PGC: (a) XRD patterns, (b) Raman spectra (c) FTIR spectra.(d)TGA curve of the Nano-Fe_3C@PGC composite, in an air flow rate of 20 mL min^{-1} at a heating rate of 10 °C min^{-1} to 800 °C.

3.2. Electrocatalytic activity of Nano-Fe_3C@PGC

The electronic conductivity and charge transfer kinetics of anodes were evaluated by electrochemical impedance spectroscopy in phosphate buffer solution (PBS) before inoculation. The obtained impedance spectra of three electrodes (Fig. 3a) are composed of a semicircle at high frequencies, corresponding to charge transfer resistance between the electrode surface and the electrolyte, and a straight-line feature at low frequencies, reflecting the limitation of Warburg diffusion. The obtained Ohm resistance (R_{ohm}) and charge transfer resistance (R_{ct}) by using the equivalent circuit (inset of Fig. 3a) are presented in Fig. 3b. The R_{ohm} mainly reveals the electronic conductivity of anode because of the highly ionic conductivity of the PBS (He and Mansfeld, 2009). It can be found from Fig. 3a and b that CF anode has a far larger R_{ohm} (33.15 Ω) than PGC (19.81 Ω) and Nano-Fe_3C@PGC (11.91 Ω). Considering the less difference in R_{ohm} between PGC and Nano-Fe_3C@PGC, the significantly reduced R_{ohm} of CF can be ascribed to the graphitized carbon in PGC. Dramatically, the CF anode has a large R_{ct} (182.7 Ω), indicating the poor electrocatalytic activity toward the charge transfer between CF and electrolyte. The R_{ct} is reduced when PGC is applied in CF, indicating the contribution of porous structure and graphitization of carbon. Nano-Fe_3C@PGC anode has a R_{ct} of 29.5 Ω, much lower than PGC anode (47.58 Ω), indicative the better electrocatalytic activity of Nano-Fe_3C@PGC toward the charge transfer. It should be noted that Nano-Fe_3C@PGC has a smaller specific surface area (169 $m^2 g^{-1}$) than PGC anode (234 $m^2 g^{-1}$). This abnormal relationship of electrocatalyst activity with specific surface area highlights the contribution of Fe_3C in Nano-Fe_3C@PGC, which might be related to the changeable valences of iron in Fe_3C (Haglund et al., 1991; Lv et al., 2008). Apparently, Nano-Fe_3C@PGC is characteristic of highly electronic conductivity and outstanding electrocatalytic activity toward the charge transfer between anode and electrolyte.

Fig. 3c illustrates the current responses of inoculated half-cells in the anolyte. The Nano-Fe_3C@PGC anode generates the notably high current density (1.77 mA cm^{-2}), much higher than CF anode (0.95 mA cm^{-2}) and PGC anode (1.46 mA cm^{-2}), implying that the Nano-Fe_3C@PGC anode has excellent electrocatalytic activity for the charge transfer between bacteria and anode. Constant-current discharge experiments were also conducted in matured half-cells. Under a constant current, the more negative potential of an anode reflects the anodic activity of the electrode (Zeng et al., 2018). As displayed in Fig. 3d, the Nano-Fe_3C@PGC anode has a more negative plateau potential (−0.545 V *vs.* SCE) than CF anode (−0.458 V *vs.* SCE) and PGC anode (−0.512 V *vs.* SCE). The CF anode has the largest polarization in MFCs because of its low degree of graphitization, small specific surface area and week electronic conductivity. The PGC anode shows a better performance than CF anode, while the Nano-Fe_3C@PGC anode exhibits a further improved performance, indicative of the contribution of Fe_3C.

3.3. Performances of MFCs based on Nano-Fe_3C@PGC

The performance of Nano-Fe_3C@PGC anode was further evaluated in single-chamber MFCs loaded with a 1000 Ω external resistance. Fig. 4a presents the voltage output of the MFCs based on Nano-Fe_3C@PGC, PGC and CF anodes, which illustrates that the MFCs exhibit reproducible cycles of voltage output after inoculation. The start-up time is about 110 h for CF anode to obtain a stable voltage of 0.45 V and 90 h for PGC anode to reach 0.55 V. Nevertheless, the Nano-Fe_3C@PGC

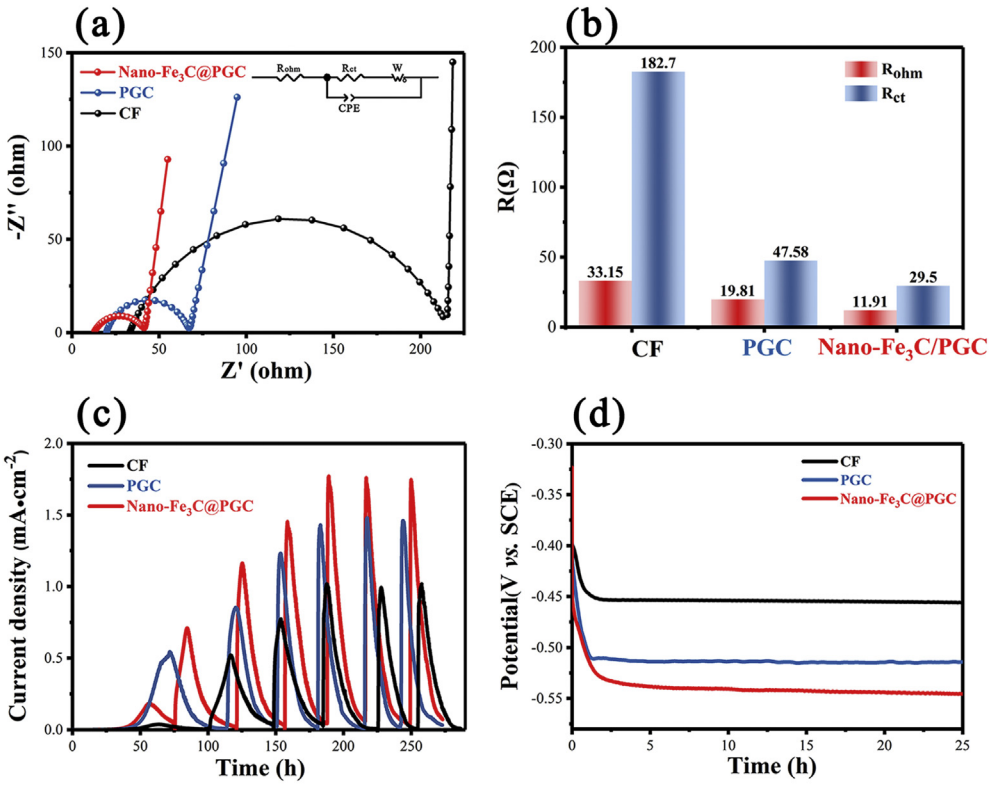

Fig. 3. Electrochemical characterizations of different anode in three electrode half-cell: (a) Electrochemical impedance spectra and equivalent circuit. (b) the fitted ohmic and charge transfer resistance of carbon felt (CF), PGC and Nano-Fe_3C@PGC electrodes in PBS before inoculation. (c) Bioelectrocatalytic current generation of different anode under a constant voltage of 0.2 V *vs.* the SCE in the acetate (1 g L^{-1}) medium solution. (d) Potential response in constant-current discharge experiments under a constant current of 0.1 μA at open circuit in the acetate medium solution after biofilm formation.

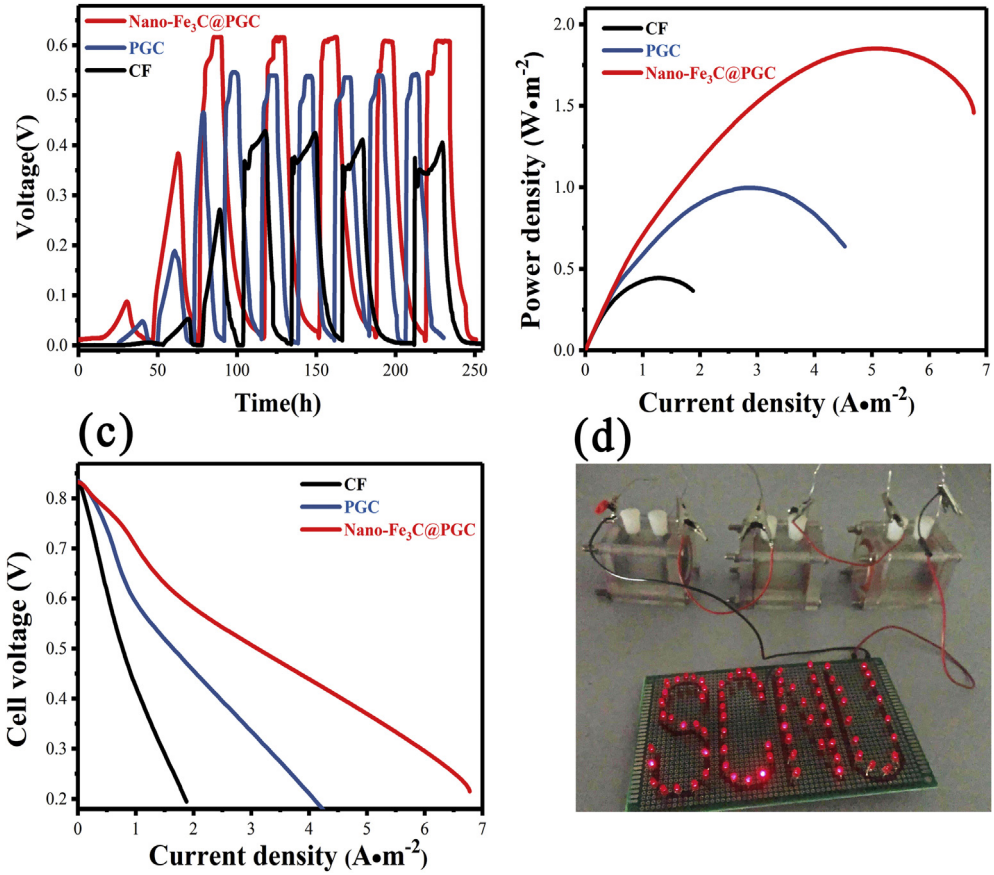

Fig. 4. Performance of the MFCs equipped with different anodes: (a) Cell voltage output during start-up with 1000 Ω resistance loading. (b) Power density, (c) polarization curves after biofilm formation for the MFCs using CF, PGC and Nano-Fe_3C@PGC anodes. (d) Digital photo of MFCs to drive 75 red LEDs with "SCNU".

anode achieves a repeatable maximum voltage (0.62 V) after inoculation for only 75 h. When the anolyte is replaced, the voltage restores quickly to the maximum value. After multiple cycles, power density curves (Fig. 4b) and polarization curves (Fig. 4c) of MFCs were measured to evaluate power generation ability. The MFC with Nano-Fe_3C@PGC anode displays the highest current intensity under the same voltage among three cells. As displayed in Fig. 4b, the MFC with Nano-Fe_3C@PGC anode generates a power density of 1856 mW m^{-2}. This power density can run 75 red Light Emitting Diodes (LEDs) with "SCNU", a thermo-hygrometer and an electromagnetical apparatus successfully (Fig. 4d, Movie S1 and Movie S2), and is 3.81-fold higher than that based on CF anode (487 mW m^{-2}) and 1.82-fold higher than that based on PGC anode (997 mW m^{-2}). The individual polarization curves of different electrodes (Fig. S11) presents that the three electrodes exert similar cathode potential but a widely different anode potential, inferring that the performance of the higher power output MFCs is mainly attributed by the anode(Chaudhuri and Lovley, 2003). These results are indicative of the importance of Nano-Fe_3C@PGC as anode electrocatalyst. Additionally, since Nano-Fe_3C@PGC can be facilely synthesized with ferrous gluconate, the cost for the preparation of Nano-Fe_3C@PGC anode is low compared to those of the anodes reported in literature (Table S2).

Supplementary data related to this article can be found at https://doi.org/10.1016/j.bios.2019.111594.

3.4. Biofilm on Nano-Fe_3C@PGC anode

The SEM images (Fig. 5a, b and 5c) show the grown biofilm on skeletons of CF, PGC and Nano-Fe_3C@PGC anodes after ten cycles' operation of Fig. 4a (about 14 days). It is visible that the bacteria covered almost the entire surface on Nano-Fe_3C@PGC and PGC electrodes, compared to the less coverage on CF anode. Confocal laser photofluorogram of bacteria are shown in Fig. 5d, e and 5f. It can be observed that the bacteria are densely adhered to the surface and inner of Nano-Fe_3C@PGC and PGC anodes, in contrast, the bacteria are inconsonant in CF anode. These differences indicate that the porous structure of Nano-Fe_3C@PGC and PGC allows for microbial attachment to guarantee the bacterial biofilm growth and yields better biocompatibility than CF.

Interestingly, Nano-Fe_3C@PGC has smaller surface area (Table S1) but exhibit better activity for electricity generation (Fig. 4) than PGC. This difference should be ascribed to the contribution of Fe_3C. To uncover the underlying mechanism, the biofilms on different anodes were performed with genus analysis and cyclic voltammetry was conducted on the anodes with and without biofilms. The microbial community in the biofilm formed after ten cycles' operation of Fig. 4a (about 14 days) was analyzed by the method described in Supplementary Materials (S1.3). The obtained results are presented in Fig. 5g and Fig. S12. As shown in Fig. 5g, the biofilms on different anode at genus level display a diverse community, including *Geobacter*, *Comamonas*, *Chryseobacterium*, etc. It is worth mentioning that Nano-Fe_3C@PGC anode has the highest amount of *Geobacter* (87%), compared to the 32% of PGC anode and the 25% of CF anode. *Geobacter* is an electrochemically active microorganism (Logan, 2009; Zhi et al., 2014), and therefore, this genus analysis suggests that the Fe_3C in Nano-Fe_3C@PGC favors the enriching of electrochemically active microorganism, which should contribute to the better performance of Nano-Fe_3C@PGC as anode of MFCs than PGC.

The anodes before the operations were performed with cyclic voltammetry in PBS solution. The shapes of the cyclic voltammograms (Fig. S13a) suggest the capacitance characteristics of all anodes, where areal capacitance (Ca mF cm^{-2}) of all electrodes has a positive correlation with the average current(Sarkar et al., 2013; Tang et al., 2015). When the capacitance comes from the electric double layer of the

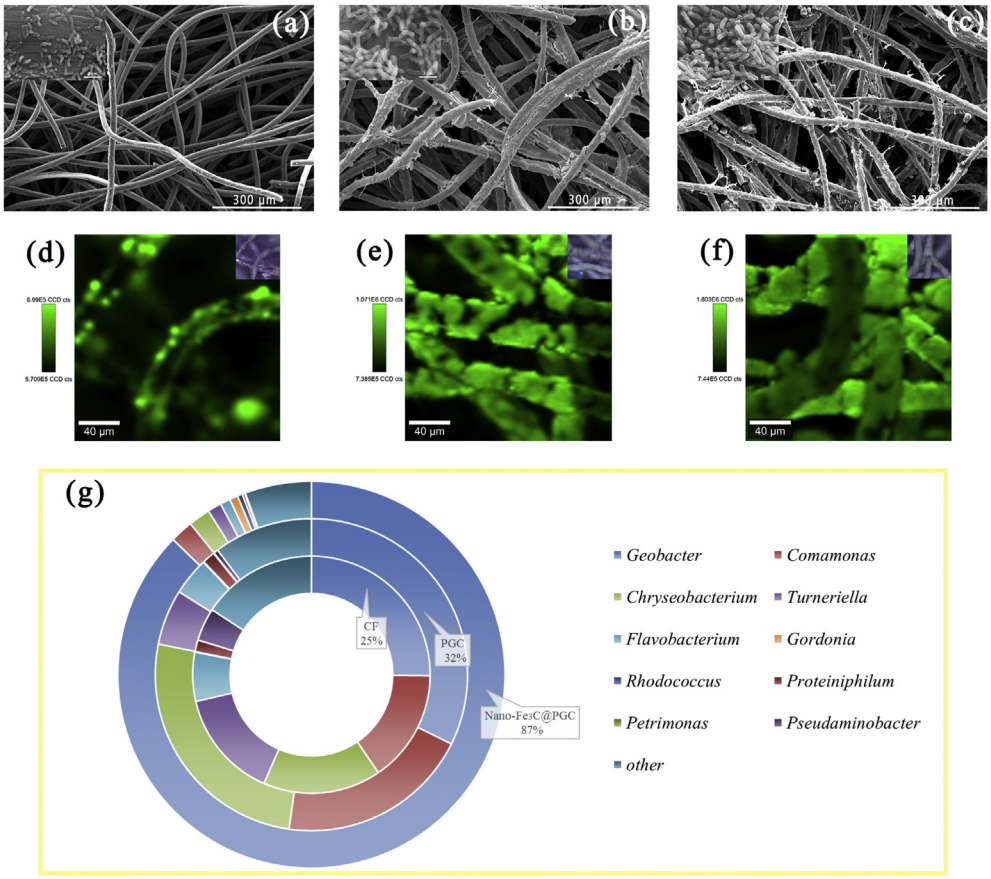

Fig. 5. SEM images of the electroactive biofilm grown on the CF (a), PGC (b) and Nano-Fe_3C@PGC (c) anodes after biofilm formation, with insets showing high resolution SEM images. confocal laser photofluorogram of bacteria on CF (d), PGC (e) and Nano-Fe_3C@PGC (f) anodes, with insets showing optical microscope photographs. (g) Structure of microbial community at different anodes.

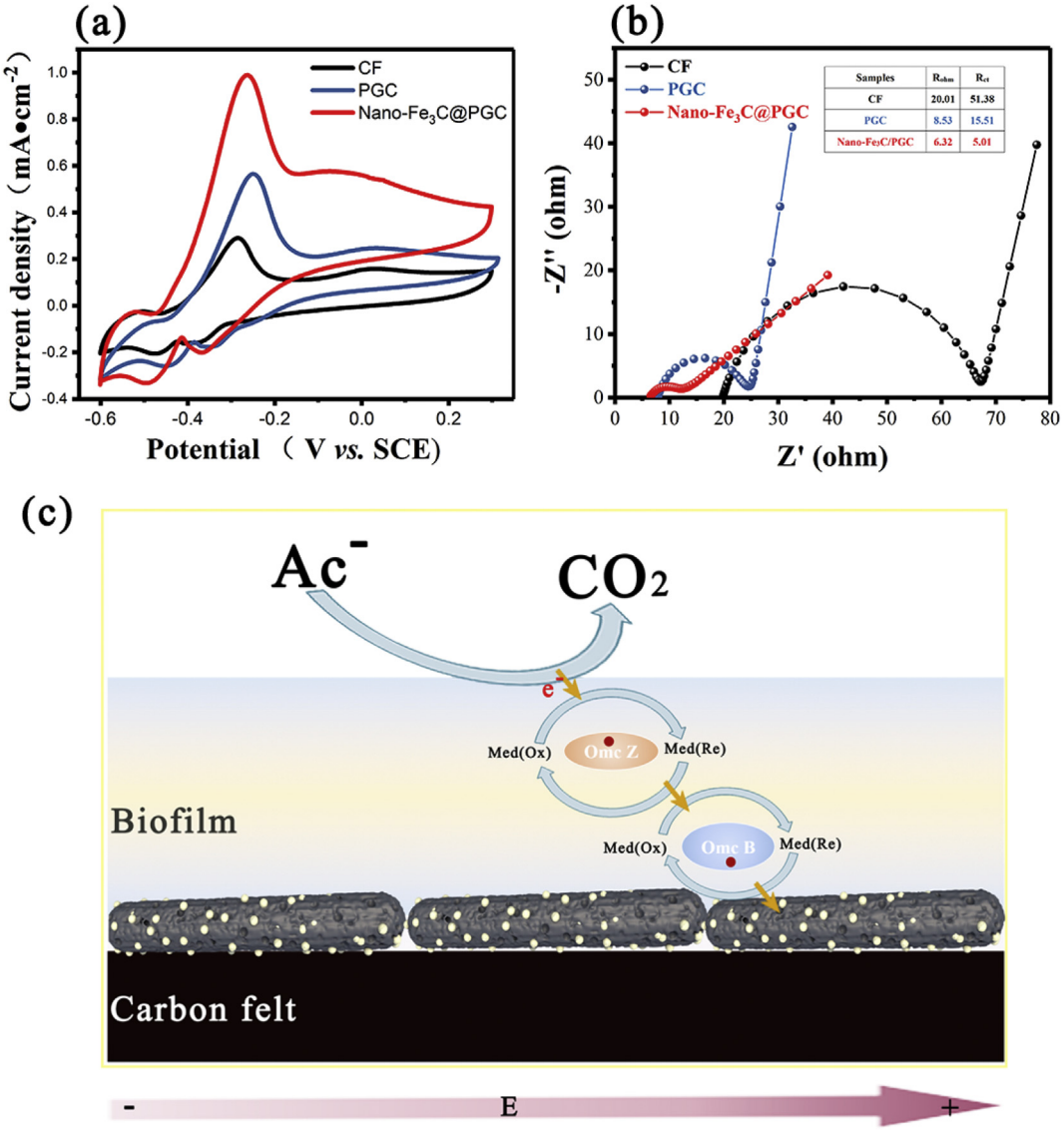

Fig. 6. (a) Cyclic voltammograms of CF, PGC and Nano-Fe_3C@PGC electrodes in the acetate medium solution. (b) Electrochemical impedance spectra under open circuit potential for the different electrodes in acetate medium solution after biofilm formation. (c) Schematic contribution of Nano-Fe_3C@PGC as anode electrocatalyst in MFCs.

electrode, it is proportional to the specific surface area (or electrochemical active surface area) of the electrode. PGC has a larger specific surface but exhibits a smaller capacitance than Nano-Fe_3C@PGC, suggesting that Fe_3C contributes to the enhanced capacitances. This contribution is well consistent with the reduced R_{ct} of PGC by Fe_3C, as observed in Fig. 3a and b. The redox reaction of iron ions in Fe_3C has a fast kinetics and takes place in the form of pseudocapacitance current.

The anodes with biofilms formed after ten cycles' operation of Fig. 4a (about 14 days) were also performed with cyclic voltammetry in PBS solution. Two redox couples can be observed from their voltammograms (Fig. S13b), which resemble other electroactive biofilms in previously reported results(Zeng et al., 2018). These two redox pairs are assigned to OmcB (outer membrane c-type cytochrome B, −0.19 V vs. SHE) and OmcZ (outer membrane c-type cytochrome Z, −0.22 mV vs. SHE)(Inoue et al., 2010; Richter et al., 2009). These cytochromes are essential for charge transfer between bacteria and anode in MFCs. The redox peak current intensity of different anodes is related to the electrocatalytic activity of the anodes toward these redox species in the biofilms (Liu et al., 2005). The larger currents of Nano-Fe_3C@PGC and PGC than CF can be ascribed to the more concentrated redox species on Nano-Fe_3C@PGC and PGC, while the larger current of Nano-Fe_3C@PGC than PGC should result from the roles of Fe_3C in the enriching of electrochemically active microorganism and the electrocatalytic activity toward redox species. It is these roles that provide MFCs based on Nano-Fe_3C@PGC anode with and outstanding power density.

As observed in Fig. 6a, the oxidation current increases but the reduction current decreases significantly when the cyclic voltammetry is performed in the acetate-containing solution on the anodes with biofilms formed after ten cycles' operation of Fig. 4a (about 14 days), demonstrating the electrocatalytic oxidation of acetate by these bioanodes (Liu et al., 2005). The maximum electrocatalytic oxidation current of the Nano-Fe_3C@PGC anode (1.01 mA cm^{-2}, normalized to the anode projected area) is far higher than those of PGC (0.56 mA cm^{-2}) and CF (0.28 mA cm^{-2}) anodes, indicative of the contribution of Fe_3C in Nano-Fe_3C@PGC. Accordingly, as shown in Fig. 6b, Nano-Fe_3C@PGC anode has a far smaller R_{ct} (5.01 Ω), than CF (51.38 Ω) and PGC (15.51 Ω) anodes.

With the results available, the electrocatalysis mechanism of Nano-Fe_3C@PGC can be illustrated schematically in Fig. 6c. Firstly, the porous structure of Nano-Fe_3C@PGC provides a large specific surface

area, which is beneficial for the formation of biofilm on anode. Secondly, Fe_3C in Nano-Fe_3C@PGC not only enriches electrochemically active microorganisms on the electrode surface but also accelerates the reactions of the redox species in microorganisms. Based on their different redox potentials, OmcB is responsible for electron transfer across the biofilm/electrode interface, while OmcZ for that between biofilm and substrate in the medium (Inoue et al., 2010; Katuri et al., 2010; Liu et al., 2008) With these contributions, the Nano-Fe_3C@PGC as anode electrocatalyst provides the MFCs with an outstanding power density. As shown in Table S3, our product Nano-Fe_3C@PGC behaves better than other porous carbon-based materials and is among the best anode of Fe-based materials that have been reported in literature.

4. Conclusions

We have successfully developed a novel anode electrocatalyst, iron carbide nanoparticles highly dispersed in porous graphitized carbon (Nano-Fe_3C@PGC), for improving the performances of microbial fuel cells. By delicately controlling the pyrolysis for carbonization of a low-cost ferrous gluconate as precursor and the acid-etching for iron species except for Fe_3C, the unique configuration of porous structure, graphitization and highly dispersed nanoparticles can be successfully achieved. Thanks to the roles that Fe_3C plays in enriching electrochemically active microorganisms and accelerating the reactions of the redox species in microorganisms, the resultant Nano-Fe_3C@PGC provides the microbial fuel cell with an outstanding power density. Considering its synthesis facileness, low-cost raw materials and outstanding electrocatalytic activity, Nano-Fe_3C@PGC is a promising anode electrocatalyst for the practical application of high-performance microbial fuel cells. Nevertheless, more investigations need to be carried out in the future, especially on the effects of the morphology and structure of Fe_3C on the activity of this electrocatalyst.

Declaration of interest statement

We declare that we do not have any commercial or associative interest that represents a conflict of interest in connection with the work submitted.

CRediT authorship contribution statement

Meihua Hu: Investigation, Writing - original draft. **Xin Li:** Investigation, Writing - original draft. **Juan Xiong:** Investigation, Writing - original draft. **Lizhen Zeng:** Investigation, Writing - original draft. **Yingshan Huang:** Investigation, Writing - original draft. **Yuping Wu:** Supervision, Writing - review & editing. **Guozhong Cao:** Supervision, Writing - review & editing. **Weishan Li:** Supervision, Writing - review & editing.

Acknowledgments

The authors are highly grateful for the financial support from National Natural Science Foundation of China (Grant no. 51471073).

Appendix A. Supplementary data

Supplementary data to this article can be found online at https://doi.org/10.1016/j.bios.2019.111594.

References

Chaudhuri, S.K., Lovley, D.R., 2003. Nat. Biotechnol. 21, 1229–1232.
Chen, S., Tang, J., Jing, X., Liu, Y., Yuan, Y., Zhou, S., 2016. Electrochim. Acta 212, 883–889.
Chen, X., Cui, D., Wang, X., Wang, X., Li, W., 2015. Biosens. Bioelectron. 69, 135–141.
Choi, S., 2015. Biosens. Bioelectron. 69, 8–25.
Cui, D., Wang, Y.Q., Xing, L.D., Li, W.S., 2014. Int. J. Hydrogen Energy 39, 15081–15087.
Dresselhaus, M.S., Jorio, A., Saito, R., 2010. Annu. Rev. Condens. Matter Phys. 1, 89–108.
Feng, C., Lv, Z., Yang, X., Wei, C., 2014. Phys. Chem. Chem. Phys. 16, 10464–10472.
Ferrari, A.C., 2007. Solid State Commun. 143, 47–57.
Guan, B.Y., Yu, L., Lou, X.W., 2016. Energy Environ. Sci. 9, 3092–3096.
Haglund, J., Grimvall, G., Jarlborg, T., 1991. Phys. Rev. B Condens. Matter 44, 2914–2919.
He, Z., Mansfeld, F., 2009. Energy Environ. Sci. 2, 215–219.
Hu, Y., Jensen, J.O., Zhang, W., Huang, Y., Cleemann, L.N., Xing, W., Bjerrum, N.J., Li, Q., 2014. ChemSusChem 7, 2099–2103.
Inoue, K., Qian, X., Morgado, L., Kim, B.C., Mester, T., Izallalen, M., Salgueiro, C.A., Lovley, D.R., 2010. Appl. Environ. Microbiol. 76, 3999–4007.
Katuri, K.P., Kavanagh, P., Rengaraj, S., Leech, D., 2010. Chem. Commun. 46, 4758–4760.
Kawale, H.D., Ranveer, A.C., Chavan, A.R., 2017. J. Biochem. Technol. 2, 1123–1127.
Li, S., Cheng, C., Thomas, A., 2017. Adv. Mater. 29, 1602547.
Liao, Y., Pan, K., Wang, L., Pan, Q., Zhou, W., Miao, X., Jiang, B., Tian, C., Tian, G., Wang, G., Fu, H., 2013. ACS Appl. Mater. Interfaces 5, 3663–3670.
Liu, H., Cheng, S., Logan, B.E., 2005. Environ. Sci. Technol. 39, 658–662.
Liu, X., Shi, L., Gu, J.D., 2018. Biotechnol. Adv. 36, 1815–1827.
Liu, Y., Harnisch, F., Fricke, K., Sietmann, R., Schroder, U., 2008. Biosens. Bioelectron. 24, 1012–1017.
Logan, B.E., Rabaey, K., 2012. Science 337, 686–690.
Logan, B.E., 2009. Nat. Rev. Microbiol. 7, 375–381.
Lv, Z.Q., Zhang, F.C., Sun, S.H., Wang, Z.H., Jiang, P., Zhang, W.H., Fu, W.T., 2008. Comput. Mater. Sci. 44, 690–694.
Malvankar, N.S., Tuominen, M.T., Lovley, D.R., 2012. Energy Environ. Sci. 5, 5790–5797.
Mian, M.M., Liu, G., 2019. Chemosphere 215, 101–114.
Niu, W.H., Li, Z., Marcus, K., Zhou, L., Li, Y.L., Ye, R.Q., Liang, K., Yang, Y., 2018. Adv. Energy Mater. 8, 1701642.
Qiao, Y., Bao, S.-J., Li, C.M., 2010. Energy Environ. Sci. 3, 544–553.
Richter, H., Nevin, K.P., Jia, H., Lowy, Daniel A., Lovleya, D.R., Tender, L.M., 2009. Energy Environ. Sci. 2, 506–516.
Samsudeen, N., Radhakrishnan, T.K., Matheswaran, M., 2015. Bioresour. Technol. 195, 242–247.
Santoro, C., Arbizzani, C., Erable, B., Ieropoulos, I., 2017. J. Power Sources 356, 225–244.
Sarkar, D., Khan, G.G., Singh, A.K., Mandal, K., 2013. J. Phys. Chem. C 117, 15523–15531.
Sonawane, J.M., Yadav, A., Ghosh, P.C., Adeloju, S.B., 2017. Biosens. Bioelectron. 90, 558–576.
Su, L., Zhou, Z., Shen, P., 2013. Electrochim. Acta 87, 180–185.
Sun, M., Davenport, D., Liu, H., Qu, J., Elimelech, M., Li, J., 2018. J. Mater. Chem. 6, 2527–2539.
Sun, M., Zhai, L.F., Li, W.W., Yu, H.Q., 2016. Chem. Soc. Rev. 45, 2847–2870.
Tang, J., Chen, S., Yuan, Y., Cai, X., Zhou, S., 2015. Biosens. Bioelectron. 71, 387–395.
Wang, W., Luo, J., Chen, W., Li, J., Xing, W., Chen, S., 2016a. J. Mater. Chem. 4, 12768–12773.
Wang, W., You, S., Gong, X., Qi, D., Chandran, B.K., Bi, L., Cui, F., Chen, X., 2016b. Adv. Mater. 28, 270–275.
Wang, X., Zhang, P., Wang, W., Lei, X., Yang, H., 2015a. RSC Adv. 5, 57828–57832.
Wang, Y.Q., Huang, H.X., Li, B., Li, W.S., 2015b. J. Mater. Chem. 3, 5110–5118.
Wang, Y., Li, B., Cui, D., Xiang, X., Li, W., 2014. Biosens. Bioelectron. 51, 349–355.
Wei, H., Wu, X.-S., Zou, L., Wen, G.-Y., Liu, D.-Y., Qiao, Y., 2016. J. Power Sources 315, 192–198.
Xiao, Y., Hwang, J.-Y., Sun, Y.-K., 2016. J. Mater. Chem. 4, 10379–10393.
Xiong, J., Hu, M., Li, X., Li, H., Li, X., Liu, X., Cao, G., Li, W., 2018. Biosens. Bioelectron. 109, 116–122.
Yu, Y.Y., Guo, C.X., Yong, Y.C., Li, C.M., Song, H., 2015. Chemosphere 140, 26–33.
Yuan, Y., Zhou, S., Liu, Y., Tang, J., 2013. Environ. Sci. Technol. 47, 14525–14532.
Zeng, L., Zhang, W., Xia, P., Tu, W., Ye, C., He, M., 2018. Biosens. Bioelectron. 102, 351–356.
Zhang, L., Liu, C., Zhuang, L., Li, W., Zhou, S., Zhang, J., 2009. Biosens. Bioelectron. 24, 2825–2829.
Zhao, F., Slade, R.C., Varcoe, J.R., 2009. Chem. Soc. Rev. 38, 1926–1939.
Zhi, W., Ge, Z., He, Z., Zhang, H., 2014. Bioresour. Technol. 171, 461–468.
Zou, L., Qiao, Y., Wu, Z.-Y., Wu, X.-S., Xie, J.-L., Yu, S.-H., Guo, J., Li, C.M., 2016. Adv. Energy Mater. 6, 1501535.